The Diurnal Cycle of Precipitation from Continental Radar Mosaics and Numerical Weather Prediction Models. Part II: Intercomparison among Numerical Models and with Nowcasting

MARC BERENGUER

Centre de Recerca Aplicada en Hidrometeorologia, Universitat Politècnica de Catalunya, Barcelona, Spain

MADALINA SURCEL AND ISZTAR ZAWADZKI

Department of Atmospheric and Oceanic Sciences, McGill University, Montreal, Quebec, Canada

MING XUE

School of Meteorology, and Center for Analysis and Prediction of Storms, University of Oklahoma, Norman, Oklahoma

FANYOU KONG

Center for Analysis and Prediction of Storms, University of Oklahoma, Norman, Oklahoma

(Manuscript received 12 July 2011, in final form 6 January 2012)

ABSTRACT

This second part of a two-paper series compares deterministic precipitation forecasts from the Storm-Scale Ensemble Forecast System (4-km grid) run during the 2008 NOAA Hazardous Weather Testbed (HWT) Spring Experiment, and from the Canadian Global Environmental Multiscale (GEM) model (15 km), in terms of their ability to reproduce the average diurnal cycle of precipitation during spring 2008. Moreover, radar-based nowcasts generated with the McGill Algorithm for Precipitation Nowcasting Using Semi-Lagrangian Extrapolation (MAPLE) are analyzed to quantify the portion of the diurnal cycle explained by the motion of precipitation systems, and to evaluate the potential of the NWP models for very short-term forecasting.

The observed diurnal cycle of precipitation during spring 2008 is characterized by the dominance of the 24-h harmonic, which shifts with longitude, consistent with precipitation traveling across the continent. Time–longitude diagrams show that the analyzed NWP models partially reproduce this signal, but show more variability in the timing of initiation in the zonal motion of the precipitation systems than observed from radar.

Traditional skill scores show that the radar data assimilation is the main reason for differences in model performance, while the analyzed models that do not assimilate radar observations have very similar skill.

The analysis of MAPLE forecasts confirms that the motion of precipitation systems is responsible for the dominance of the 24-h harmonic in the longitudinal range 103°–85°W, where 8-h MAPLE forecasts initialized at 0100, 0900, and 1700 UTC successfully reproduce the eastward motion of rainfall systems. Also, on average, MAPLE outperforms radar data assimilating models for the 3–4 h after initialization, and nonradar data assimilating models for up to 5 h after initialization.

1. Introduction

Some authors (e.g., Fritsch and Carbone 2004; Knievel et al. 2004) have proposed the evaluation of numerical weather prediction (NWP) forecasts in terms of how well they reproduce statistical properties of observations as an alternative to skill scores based on point-to-point comparison. In this sense, Dai et al. (1999), Davis et al. (2003), Dai and Trenberth (2004), Knievel et al. (2004), Janowiak et al. (2007), Clark et al. (2007, 2009), and others have performed such evaluations by examining how NWP models depict the diurnal cycle of precipitation during the warm season over North America. Their analyses are indicative of model performance in characterizing

Corresponding author address: Madalina Surcel, 805 Sherbrooke St., W #945, Montreal QC H3A 2K6, Canada.
E-mail: madalina.surcel@mail.mcgill.ca

DOI: 10.1175/MWR-D-11-00181.1

convection initiation, the motion of organized convection, and the convection related to sea-breeze circulations near the Gulf of Mexico. Similarly, in a recent paper (Surcel et al. 2010, hereafter Part I) we have evaluated the performance of the Canadian Global Environmental Multiscale (GEM) model in terms of its depiction of the diurnal cycle of precipitation, focusing on the performance of the model in different precipitation regimes.

This second part focuses on comparing the skill of different models in depicting the diurnal cycle of precipitation and in forecasting rainfall during spring 2008. For this purpose, in addition to the precipitation outputs of the operational version of the GEM model (Côté et al. 1998; Mailhot et al. 2006) already presented in Part I, this study also analyzes precipitation forecasts from the Storm-Scale Ensemble Forecast (SSEF) system developed by the University of Oklahoma's Center for Analysis and Prediction of Storms (CAPS; Xue et al. 2008; Kong et al. 2008; Coniglio et al. 2010). The SSEF was run as part of the 2008 National Oceanic and Atmospheric Administration (NOAA) Hazardous Weather Testbed (HWT) Spring Experiment with a grid spacing of 4 km and it explicitly depicts convection. In contrast, GEM was run on a significantly coarser grid (15 km) with convective parameterization. Given that convective activity is one of the main agents determining the diurnal cycle of precipitation, especially during summer [as shown, among others, by Carbone et al. (2002) or in Part I], we expect the representation of convection to play an important role in model performance.

This study also includes precipitation forecasts produced by the McGill Algorithm for Precipitation Nowcasting Using Semi-Lagrangian Extrapolation (MAPLE), described in Germann and Zawadzki 2002). MAPLE is a nowcasting system based on extrapolating recent observations by Lagrangian persistence and is thus not able to handle precipitation growth and decay. Previous long-term evaluations of MAPLE (Kilambi and Zawadzki 2005; Lin et al. 2005; Germann et al. 2006) have indicated a skill superior to NWP models for the first 6 h. The purpose of including MAPLE in this study is to quantify how much of the diurnal cycle can be explained by the motion of precipitation systems, and to serve as a reference for the evaluation of the radar data assimilating SSEF members in the context of precipitation nowcasting.

The paper is structured as follows: first, the analyzed dataset is presented (section 2). Section 3 evaluates the skill of the analyzed NWP models in reproducing the diurnal cycle of precipitation. Similarly, section 4 focuses on MAPLE's depiction of the diurnal cycle. The dependence of the quality of the deterministic forecasts on the time of day is analyzed in section 5. Finally, the main findings of the study are summarized in section 6.

2. Data description

a. Model precipitation forecasts

The CAPS SSEF is a state-of-the-art storm-scale ensemble forecasting system that was run as a contribution to the 2008 NOAA HWT Spring Experiment from April to June 2008 (Xue et al. 2008; Kong et al. 2008). The system uses the Advanced Research version of the Weather Research and Forecasting model (ARW-WRF; Skamarock et al. 2008), version 2.2, and consists of 10 members with different physical schemes and perturbed initial and lateral boundary conditions (IC–LBC). The 30-h forecasts starting at 0000 UTC are run for each member on a 4-km grid. The background ICs are interpolated from the North American Mesoscale Model (NAM; Janjic 2003) 12-km analysis, and ICs perturbations for perturbed members are obtained from the operational Short-Range Ensemble Forecast (SREF; Du et al. 2006) system from the National Centers for Environmental Prediction (NCEP) Environmental Modeling Center (EMC). Convective-scale observational information is introduced into the ICs of nine of the members by assimilating level-II radial velocity and reflectivity data from individual Weather Surveillance Radar-1988 Doppler (WSR-88D) radars and data from surface station networks. Radar data are treated with the CAPS processing package that includes a quality control and averaging of radar observations from their native coordinates onto the 4-km model grid (superobing). The data are then assimilated with a three-dimensional variational data assimilation (3D-Var) cloud analysis system (Gao et al. 2004; Brewster et al. 2005; Hu et al. 2006a,b) within the Advanced Regional Prediction System (ARPS; Xue et al. 2003). A basic description of the model configuration can be found in Tables 1 and 2 (for more information see Xue et al. 2008; Kong et al. 2008). Two of the members (control members C0 and CN) do not have SREF-based IC–LBC perturbations, have identical model configurations, and use interpolated NAM analyses as background for ICs. However, convective-scale observations from radar and surface stations are assimilated only within CN. In this article, we analyze deterministic forecasts from C0, CN, N2, and the probability-matched ensemble mean. The N2 member has the same configuration as CN, but with perturbed IC–LBC. The probability-matched SSEF mean (hereafter PM mean) is generated as proposed by Ebert (2001) by imposing the frequency distribution of rainfall intensities from the nine ensemble members assimilating radar data (i.e., all except C0) to the traditional ensemble mean (the average of these ensemble members). The probability matching has been applied on a domain slightly larger than the analysis domain presented in Fig. 1. In this way,

TABLE 1. Summary of model configurations. Planetary boundary layer (PBL) schemes: moist turbulent kinetic energy (moist TKE; Mailhot et al. 2006) and Mellor–Yamada–Janjic turbulence parameterization scheme (MYJ; Janjic 2001). Cumulus parameterizations: Kain–Fritsch cumulus parameterization scheme (KF; Kain and Fritsch 1990, 1993) and Kuo-transient convection scheme (Bélair et al. 2005). Radiation schemes: Goddard shortwave radiation scheme (Tao et al. 2003) and Rapid Radiative Transfer Model (RRTM; Mlawer et al. 1997). Land surface models: interactions between Soil–Biosphere–Atmosphere scheme (ISBA; Bélair et al. 2003a,b) and the Noah land surface model (Ek et al. 2003).

Model	GEM15	SSEF
Reference	Mailhot et al. (2006)	Xue et al. (2008)
Horizontal grid spacing	15 km	4 km
Initial conditions	Regional data assimilation system	NAM12 0000 UTC
PBL scheme	Moist TKE	MYJ
Cumulus parameterization	KF–Kuo-transient	—
Cloud microphysics	Sundqvist (1978)	Thompson et al. (2008)
Shortwave radiation scheme	Fouquart and Bonnel (1980)	Goddard
Longwave radiation scheme	Garand (1983)	RRTM
Land surface model	ISBA	Noah

over the domain on which it is computed, the PM mean has the distribution of rainfall intensities predicted by the nine ensemble members. However, this is not necessarily the case when the coverage is computed over smaller subdomains. This procedure assumes that the correct location of rainfall is well depicted by the ensemble mean and that the ensemble members give the correct frequency distribution of rainfall intensities.

GEM [Table 1; see a complete description in Mailhot et al. (2006) and references therein] is a global, hydrostatic, variable-resolution model, used operationally at the Canadian Meteorological Center (CMC) for regional forecasting since May 2004. In the central part of the domain, which covers North America, the horizontal grid spacing is uniform at 15 km and the vertical grid spacing is variable with 58 vertical levels and with the model lid being at 10 hPa. It is run twice a day, at 0000 and 1200 UTC, and the ICs are provided by a 3D-Var Regional Data Assimilation System (RDAS; Laroche et al. 1999) that does not include radar observations. The GEM model employs the Kuo transient scheme for shallow convection (Bélair et al. 2005) and the Kain and Fritsch (1990) scheme for deep convection. In this study we analyze 30-h precipitation forecasts of hourly rainfall accumulations starting from 0000 UTC. We refer to this model configuration as GEM15.

b. Radar data

As in Part I, the verification data consist of U.S. radar mosaics at 2.5-km altitude generated by the National Severe Storm Laboratory (NSSL; Zhang et al. 2005) every 5 min and with a resolution of 1 km in space.

A threshold of 15 dBZ is used to discriminate between raining and nonraining areas for the computation of rainfall coverage, and maps of reflectivity Z are converted into rain rate R according to $Z = 300R^{1.5}$. Instantaneous rainfall intensity maps every 15 min have been averaged to obtain maps of hourly accumulated rainfall.

TABLE 2. Configuration of the different SSEF members. Only C0, CN, and N2 (in boldface) have been used in this study. CN and C0 are control members and the rest have perturbed initial and lateral boundary conditions (IC–LBC). The microphysics schemes include Thompson (Thompson et al. 2008), WRF Single-Moment 6-class (WSM6; Hong and Lim 2006), and Ferrier (Ferrier et al. 2002). Some members use the Goddard shortwave radiation scheme (Tao et al. 2003) and the rest use the Dudhia (1989) scheme. The abbreviations for the PBL schemes are the Mellor–Yamada–Janjic (MYJ; Mellor and Yamada 1982; Janjic 2003) and the Yonsei State University (YSU; Noh et al. 2003).

Member	Radar data assimilation	IC–LBC perturbations	Microphysics	Shortwave radiation scheme	PBL scheme
CN	**Yes**	**No**	**Thompson**	**Goddard**	**MYJ**
C0	**No**	**No**	**Thompson**	**Goddard**	**MYJ**
P1	Yes	Yes	WSM6	Dudhia	MYJ
P2	Yes	Yes	WSM6	Dudhia	YSU
P3	Yes	Yes	Ferrier	Goddard	MYJ
P4	Yes	Yes	Thompson	Dudhia	YSU
N1	Yes	Yes	Ferrier	Goddard	YSU
N2	**Yes**	**Yes**	**Thompson**	**Goddard**	**MYJ**
N3	Yes	Yes	Thompson	Dudhia	YSU
N4	Yes	Yes	WSM6	Goddard	MYJ

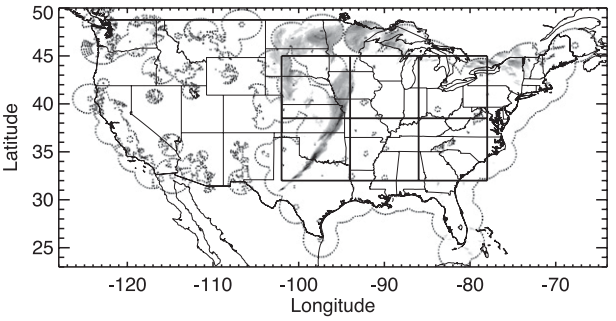

FIG. 1. Analysis domain. The dotted circles represent the coverage of the 2.5-km CAPPI maps, while the rectangles ranging from 32°–45°N to 103°–78°W correspond to the subdomains on which the statistics have been computed. The precipitation field presented in this figure is typical for spring 2008.

c. *MAPLE forecasts*

MAPLE (see a complete description in Germann and Zawadzki 2002) is an extrapolation-based technique for precipitation nowcasting. It uses the Variational Echo Tracking (VET) algorithm (Laroche and Zawadzki 1995) to estimate the motion field of precipitation, and a modified semi-Lagrangian backward scheme for advection.

Here, MAPLE has been run using the NSSL 2.5-km rainfall maps described above to generate 8-h forecasts initialized every hour with a horizontal resolution of 1 km and a sampling in time of 15 min.

d. *Cases studied and analysis domain*

The forecasts and observations employed in this study have different resolutions, domains, and time periods of availability. Except when specified otherwise, the analyses have been carried out over six subdomains covering most of central and eastern United States from 103° to 78°W in longitude and from 32° to 45°N in latitude as illustrated in Fig. 1. As in Part I, the analysis focuses on forecasts of hourly rainfall accumulations initialized at 0000 UTC. The precipitation forecasts have been remapped onto a common 4-km, latitude–longitude grid using nearest-neighbor interpolation. The remapped fields are then smoothed to a 32-km resolution using a Haar wavelet low-pass filter.

We have studied 24 precipitation cases from 16 April to 6 June 2008 when 30-h forecasts from all model runs were available (see details in Table 3).

TABLE 3. Case studies.

Month	Days
Apr 2008	18, 23, 24, 25, and 30
May 2008	1, 2, 5, 6, 7, 8, 19, 20, 21, 22, 24, 27, 28, 29, and 30
Jun 2008	2, 4, 5, and 6

3. Model depiction of the diurnal cycle of precipitation during spring 2008

a. *Mean diurnal cycle of precipitation*

As discussed in Part I, the diurnal cycle of precipitation during spring 2008 as depicted from radar observations is characterized by rainfall systems that demonstrate some consistency in their timing and evolution, initiating on average around 103°W at 1900 UTC, and propagating along a time–longitude corridor to 85°W at 0600 UTC. However, these radar observations do not show the characteristic signal associated with stationary afternoon convection induced by thermal forcing in the southeastern part of the domain, usually present during summer (Carbone et al. 2002; Part I). Instead, little precipitation is observed in the eastern portion of the domain (for more details on the diurnal cycle of precipitation during spring 2008 and on its seasonal and interannual variability, the reader is directed to Part I).

Unlike during summer 2008, GEM15 possesses some skill in reproducing the mean diurnal cycle of precipitation during spring 2008. GEM15 forecasts reproduce the characteristic west–east precipitation corridor, but the rainfall coverage and to a lesser extent the rainfall amounts are overestimated. This result can also be observed in Figs. 2 and 3, which show the mean evolution of precipitation coverage and of hourly rainfall intensities over the domains described in section 2 as a function of lead time (and consequently UTC time as the forecasts are initialized at 0000 UTC). It is worth noticing that although GEM clearly overestimates precipitation coverage, average rainfall intensities (Fig. 3) do not present large biases.

The other model configurations also overestimate precipitation coverage, GEM15 and C0 being the least biased. In terms of the mean hourly rainfall intensity, the model–radar comparison shows a geographical dependence: while in the westernmost domains the 4-km SSEF members seem to best agree with the observations and GEM15 underpredicts the rainfall amounts, in the central and eastern regions C0 and CN overpredict precipitation and GEM15 is the closest to observations (cf. the different lines in Fig. 3).

Others (e.g., Weisman et al. 2008; Schwartz et al. 2009; 2010) have shown similar overprediction of rainfall coverage and amounts using 4-km, convection-allowing versions of WRF, similar to the SSEF members analyzed here. In particular, Schwartz et al. (2010), when studying the sensitivity of the results to the planetary boundary layer (PBL) parameterizations, reported larger biases for the members using the Mellor–Yamada–Janjic (MYJ)

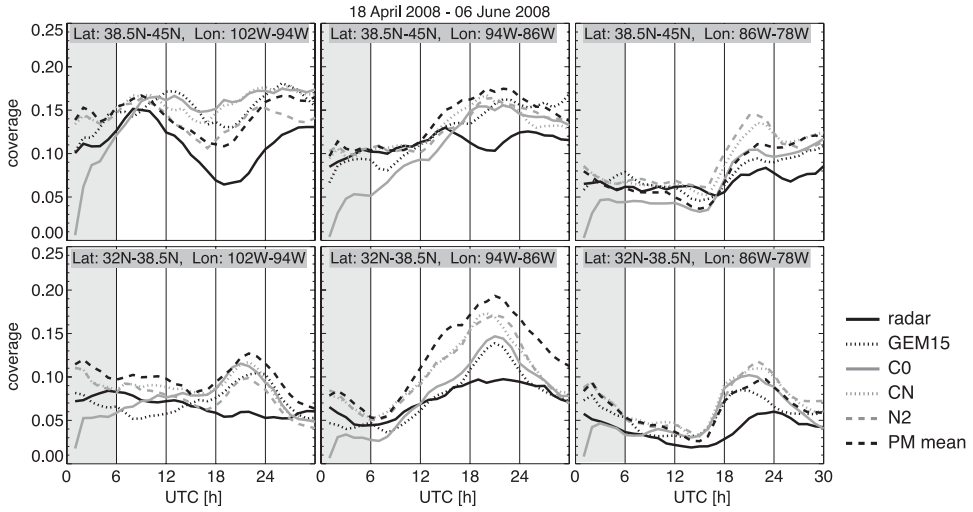

FIG. 2. Regional diurnal cycle of fractional precipitation coverage (using a threshold of 0.2 mm h^{-1}) over the subdomains of analysis (see Fig. 1) for the entire period of analysis for radar observations and for the different rainfall outputs as indicated on the legend. The order of the graphs corresponds to the geographic position of the domains.

scheme (present in the three SSEF members selected here; Table 2), and lesser biases for the members using the YSU option. The latter is used in other SSEF members not included in our analysis.

The only difference between the configurations of SSEF control members C0 and CN is in the initialization (Table 2), the ICs for C0 being simply interpolated from the NCEP NAM analysis, while CN is benefiting from an advanced data assimilation system that includes radar observations. As mentioned by Kain et al. (2010), while the assimilation of other mesoscale observations is also important, radar data assimilation plays the dominant role in the simulation of deep convection. Therefore, the comparison between C0 and CN allows us to investigate the impact of assimilating radar data, which both Xue et al. (2009) and Kain et al. (2010) indicate as significant within the first 9–12 h of the forecasts. Figure 2 confirms a delay in the onset of precipitation with C0 relative to CN: in the northwest, C0 forecasts reach the rainfall coverage forecasted by CN after 8 h, while in other regions (e.g., in the south-central and northeastern domains), this point is not reached even after 24 h.

The comparison of CN with N2 highlights the effect of IC–LBC perturbations in depicting the diurnal cycle of precipitation. The results presented in Figs. 2 and 3 are mostly in agreement with the findings of Schwartz

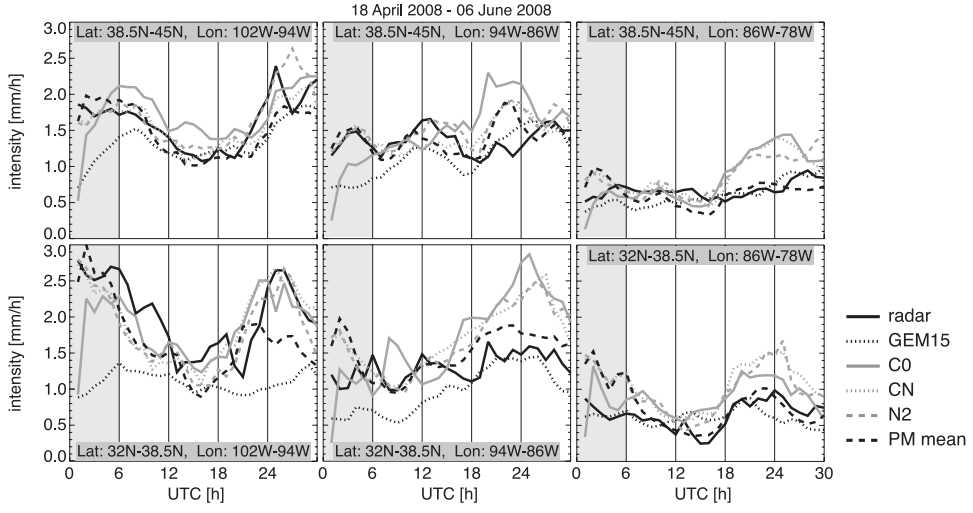

FIG. 3. As in Fig. 2, but for the average hourly rainfall intensity.

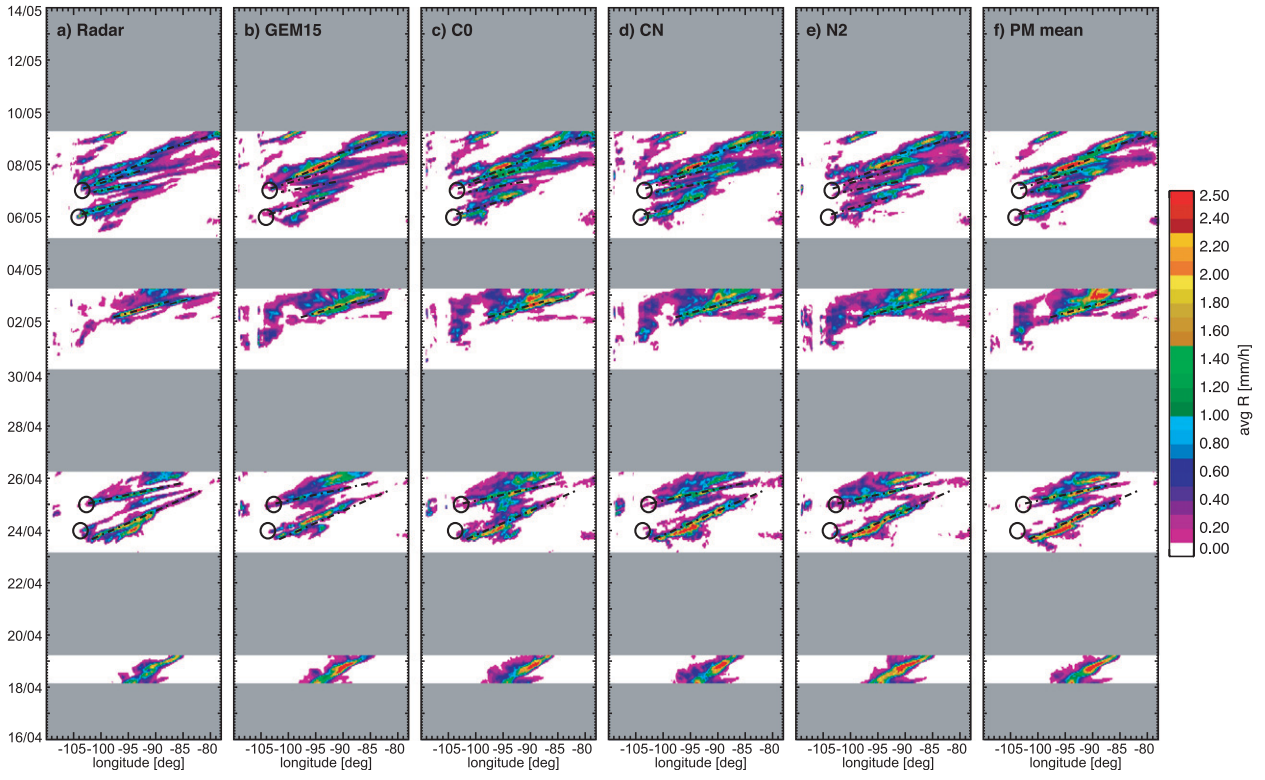

FIG. 4. Hovmöller time series of average rain intensity (mm h^{-1}) for (from bottom to top) 16 Apr–14 May averaged in the latitudinal range 32°–45°N for (a) radar observations and (b)–(f) the 6–30-h model forecasts run at 0000 UTC: GEM15; SSEF members C0, CN, and N2; and the PM mean. The longitudinal range extends from 110° to 78°W (notice that it is larger than that in Fig. 1). The ticks in the *y* axis correspond to 0000 UTC, and the gray shading represents the days when no data were available. The circles indicate the location and timing of convection initiation and the dashed–dotted lines are centered along precipitation streaks. Both the circles and the dashed lines have been obtained by subjective analysis of radar observations and are overlaid on the model diagrams of (b)–(f) to enable comparison.

et al. (2010), who showed little differences between the mean diurnal evolution of coverage and rainfall intensity of the members with the same microphysics and PBL parameterizations.

Finally, for the first forecast hour, the PM mean shows average values of coverage and rainfall intensity (Figs. 2 and 3) similar to CN, N2, and radar observations. This is because all the SSEF members except C0 assimilate radar data and hence the precipitation patterns forecasted during the first hour by the members (not shown) are very similar to the observed, thereby constraining the spread of the ensemble. However, with lead time, the PM mean predicts coverage and rainfall intensity values different than those of the CN and N2 members presented here, particularly in the central and western subdomains. This is mostly caused by the fact that some ensemble members (not shown) forecast higher average coverage and intensity values than CN and N2, which Schwartz et al. (2010) attributed to the different PBL and microphysical parameterizations used (listed in Table 2).

b. Time–longitude diagrams

Figures 4 and 5 show the Hovmöller (time–longitude) diagrams of hourly rainfall accumulations from radar observations and from model forecasts for lead times between 6 and 30 h; the first 6 h of the forecasts have been ignored to avoid the spinup time of the models. These have been obtained, as in Part I, by averaging hourly rainfall intensities within the latitudinal range 32°–45°N. In these plots, organized rainfall systems appear as time–longitude precipitation ''streaks,'' the slope of these streaks indicating the apparent zonal speed (e.g., Carbone et al. 2002; Part I). Visual inspection reveals that during spring 2008, most of the analyzed precipitation systems (e.g., 23–24 April, 2 and 6–8 May, and 4–5 June 2008) originated from convective cells on the lee side of the Rockies, which then organized along large-scale features and crossed the continent in about 24 h. This is different than during summer, when precipitation systems organize at smaller scales and the extent of west–east streaks is shorter (lasting for about 12 h; see Part I; Carbone et al. 2002).

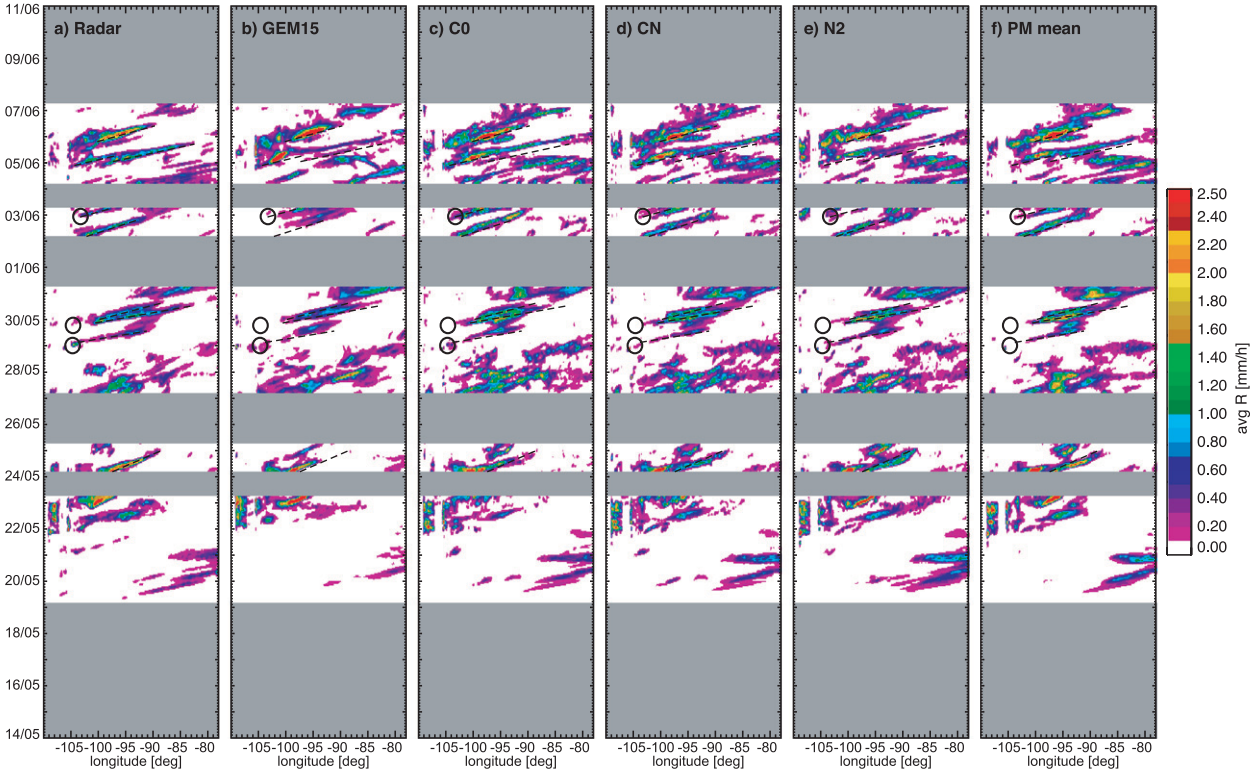

FIG. 5. As in Fig. 4, but for 14 May–11 Jun 2008.

Overall, except for the general overestimation of rainfall amounts also identified in section 3a, all forecasting systems are able to adequately depict the evolution of precipitation during spring 2008 with very few rainfall events being missed. However, a more careful analysis of the Hovmöller diagrams uncovers some clear errors in forecasting (i) the location and timing of convection initiation in the western portion of the domain (encircled in Figs. 4 and 5) and (ii) the timing, duration, and speed of the precipitation streaks (marked with dashed–dotted lines in Figs. 4 and 5).

These errors have a direct impact on the Hovmöller diagrams of the average diurnal cycle of precipitation coverage and intensity presented in Fig. 6. These have been obtained by averaging rainfall occurrence and hourly intensities of all events within the latitudinal range of 32°–45°N and as a function of time of the day. The models reproduce well the average timing of precipitation initiation along the foothills of the Rockies at about 1900 UTC (indicated by a small circle in Fig. 6), as well as the time–longitude corridor along which precipitation systems cross the continent (marked by an ellipse in Fig. 6). However, the average Hovmöller diagrams for all model configurations exhibit a weaker signal along this corridor (this problem seems less significant for the radar data assimilating SSEF members) and show additional streaks that are apparent in both the coverage and rainfall intensity panels. We attribute these features to nonsystematic errors in NWP models in reproducing the timing, location, and motion of precipitation.

There are some clear similarities between the mean diurnal Hovmöller diagrams for the three SSEF members (Figs. 6c–f, i–l). They satisfactorily replicate the time–longitude corridor of precipitation, but they all fail to dissipate the systems traveling eastward beyond 92°W after 1500 UTC. It is quite apparent that, on average, simulated systems are much larger and more intense than those depicted by radar observations. In addition, the Hovmöller diagrams for the models show two maxima around 2000 UTC at longitudes 95° and 90°W that are not present in those computed from radar observations. On the other hand, the visual comparison of the Hovmöller diagrams for C0 and CN reveal some differences in their representation of the main precipitation streak between 0600 and 1500 UTC (marked with an ellipse in Fig. 6), CN depicting better than C0 the amplitude of the diurnal cycle between 97° and 92°W. However, the model–radar correlation coefficients computed in the Hovmöller domain are very similar for the three members. To assess the significance of these correlation coefficients, statistical tests have been performed by adapting the resampling methodology presented by Hamill (1999). For two given

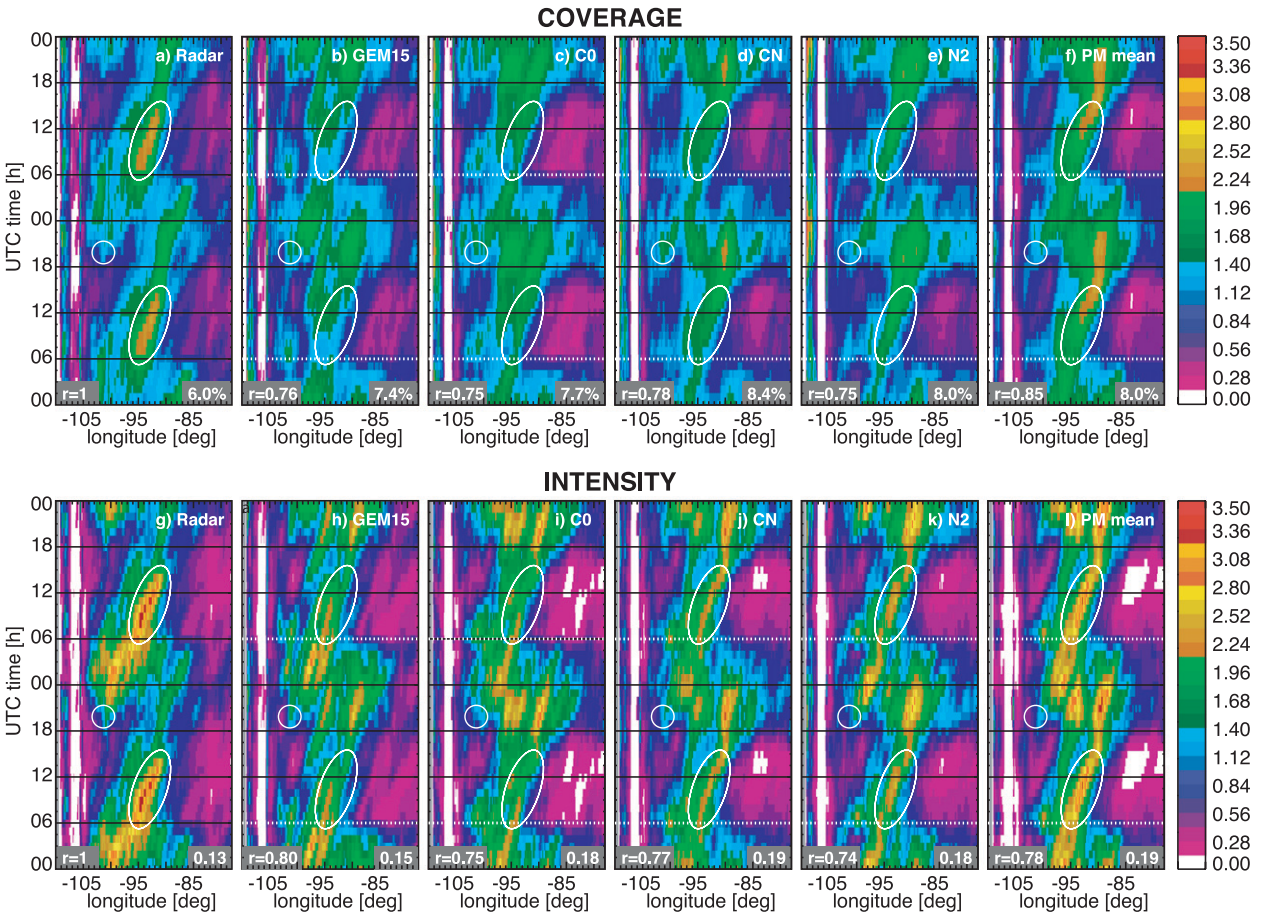

FIG. 6. Hovmöller diagrams of the average diurnal cycle of precipitation in the latitudinal range 32°–45°N for the period 16 Apr–6 Jun 2008 generated from the 6–30-h forecasts initialized at 0000 UTC. The longitudinal range extends from 110°–78°W. The diagrams are duplicated along 0000 UTC, and the white dashed lines at 0600 UTC indicate the range of the 6–30-h forecasts (note that in the range 0000–0600 UTC, the 24–30-h forecasts have been employed). The (a)–(f) precipitation coverage and (g)–(l) intensity computed from the source indicated in each. The Hovmöller diagrams are normalized (divided) by the corresponding average coverage and rainfall intensity values that are indicated in the bottom-right corner of each diagram (in % for coverage and in mm h^{-1} for rainfall intensity). In the bottom-left corner of (a)–(l) r is the correlation between the Hovmöller diagram and that obtained from radar observations. The small circle indicates the timing and location of convection initiation on the west side of the analysis domain, and the ellipse covers part of the main precipitation streak that is well depicted by SSEF members assimilating radar data (see the text).

models, a resampled set has been constructed by randomly choosing the daily Hovmöller diagram of either one or the other model for each day. A second resampled set was constructed using the data not included in the first. From these two resampled sets (artificial time series) we have computed the mean daily time–longitude diagrams (say H1 and H2, similar to those in Fig. 6), and we have calculated the correlation coefficients between each of them and the Hovmöller diurnal cycle of radar observations (Figs. 6a,g). Since H1 and H2 have been constructed by randomly picking the forecasts from either model for each day, the difference between the correlation coefficients is expected to be 0. The process described above has been repeated 1000 times, thus obtaining a distribution of correlation differences. From this distribution the intervals for significance level $\alpha = 0.05$ have been estimated, showing that the differences in the correlation coefficients among C0, CN, and N2 are not statistically significant.

The Hovmöller diagrams of the PM mean (Figs. 6f,l) reveal a higher correlation with observations (Figs. 6a,g) than any of the 10 individual members. The resampling methodology described above showed that the higher correlation corresponding to the PM mean is significant for 8 out of the 10 SSEF members for precipitation coverage. This means that the PM mean succeeded in smoothing the timing and location errors of the individual members (similar results were found by Clark et al. 2009). In this sense, the PM mean optimally represents the rainfall maxima at 1000 UTC along longitude 93°W and

at 0000 UTC along longitude 98°W. However, it suffers from the same aforementioned problems of the individual SSEF members; namely, an extended duration of traveling systems and the existence of two rainfall maxima beyond 2000 UTC. Finally, the Hovmöller diagrams of the PM mean resemble more those of GEM15 (with a correlation coefficient between the diagrams of Figs. 6h,l of 0.88), than those of observations (the correlation between radar observations and the PM mean Figs. 6g,l, respectively, is 0.78). This indicates that these NWP precipitation forecasts, notwithstanding differences in model configurations, physical parameterizations, etc., are more similar to each other than to observations, hence suggesting similar fundamental difficulties in the depiction of the diurnal cycle of precipitation by NWP models.

The results presented so far in this section are for lead times in the range 6–30 h. Surcel et al. (2009) presented the analysis of Hovmöller diagrams derived from NWP forecasts in the range 0–24 h from the same dataset. The main differences with the current results are (i) a discontinuity at 0000 UTC with GEM and C0 because of the time needed to develop precipitation in their initialization process, and (ii) the better depiction of the precipitation corridor in the 0000–0600 UTC time interval by the SSEF members that are assimilating radar observations.

c. *Frequency analysis of daily averaged Hovmöller diagrams*

In Part I, a Fourier analysis on the average Hovmöller diagrams of precipitation coverage and average rainfall intensity has been performed to identify the important modes of diurnal variability and to evaluate GEM15's ability to represent them. Similarly, Fig. 7 illustrates the normalized power spectra of the average Hovmöller diagrams of rainfall intensity (Fig. 6) for radar observations and model forecasts, while Fig. 8 portrays the phases of the 24-h harmonics as function of longitude.

Radar observations indicate the dominance of the 24-h harmonic across the continent, and especially in the range 103°–92°W, where it explains at least 90% of the variance. Between 103° and 100°W, the 24-h harmonic depicts the recurrent nature of convection initiation and shows a nearly constant phase with longitude in Fig. 8 (the black line is nearly horizontal between 103° and 100°W). On the other hand, between 100° and 84°W where the motion of precipitation systems is the main mechanism of precipitation occurrence, the phase of the 24-h harmonic shifts with longitude as indicated by the slope of the black line in Fig. 8. Even though the 12- and 8-h harmonics appear more dominant in the range 92°–83°W (Fig. 7), the origin of these harmonics in spring is not clear. Visual inspection of precipitation patterns in Figs. 4 and 5 would suggest that the dominance of the 24-h harmonic east of 83°W cannot be attributed to the well-documented stationary diurnal cycle of convection induced by thermal forcing in the southeastern United States during the warm season (Carbone et al. 2002; Part I), but rather to the arrival of systems from the west.

As also discussed in Part I, the discrepancies between the models and radar power spectra are regarded as a result of the inability of the NWP models to capture the time–space consistency of precipitation systems. In the range 103°–92°W, all models have generated some excessive power at the higher-frequency harmonics (Figs. 7b–f). This is the consequence of the presence of more streaks in the precipitation corridor for the forecasts than observed (due to the errors described in section 3b), which results in reduced power at the 24-h harmonic. For the SSEF members, this is particularly visible east of 95°W, associated with the appearance of the local maxima around 2000 UTC (Fig. 6). East of 92°W, all systems seem to attribute more power to the 24-h harmonic than what is actually present in observations. In particular, the SSEF members show the dominance of the 24-h harmonic between 92° and 78°W as a result of the clear overestimation of the duration of the systems mentioned above.

In terms of the phase of the 24-h harmonic, all models capture well the timing of the diurnal maximum between 103° and 98°W (Fig. 8), even though the amplitude of this maximum is underestimated in the simulations. In the range 98°–94°W the models forecast the timing of the diurnal maximum 2–4 h earlier than observed. It thus appears that the models have a delay in the development of convection, as confirmed by Fig. 6 where the observed diurnal maximum at 98°W at 0000 UTC is shifted to the east in the simulated diurnal cycles. Therefore, between 98° and 94°W, the variation of the phase of the 24-h harmonic with longitude for the NWP models is caused by the development of precipitation whose timing varies slowly with longitude. Between 94° and 90°W, the 24-h harmonic does not explain much of the variance (see Fig. 7) and, therefore, it is difficult to interpret the variation of the phase of this harmonic with longitude. Within 90°–85°W, all models anticipate the timing of the diurnal maximum by 2–3 h. The differences are less significant east of 85°W because of the reduced rainfall observed during the analysis period.

4. MAPLE's depiction of the diurnal cycle

MAPLE forecasts the evolution of the rainfall field by extrapolating the most recent radar observations with the motion field estimated in the immediate past. According

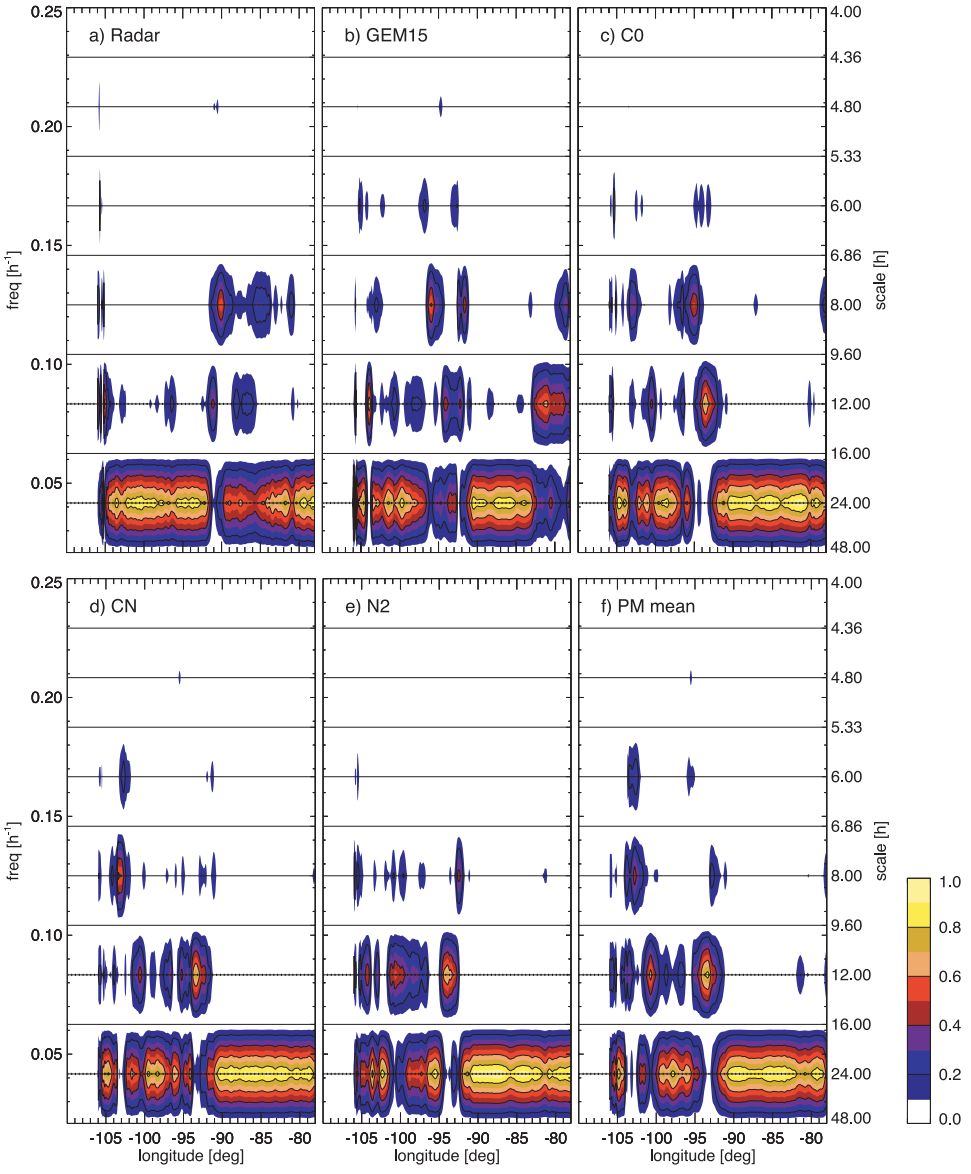

FIG. 7. Normalized power spectrum of the Hovmöller diurnal cycle of average hourly rainfall intensity from the indicated sources of data as function of longitude for the period 16 Apr–6 Jun 2008.

to Germann et al. (2006), this motion is attributed to a combination of the steering level winds transporting the precipitation systems and of the apparent motion resulting from systematic growth and decay. Therefore, unlike NWP models, MAPLE cannot be expected to reproduce the changes in rainfall intensities due to other mechanisms (e.g., initiation and dissipation of convective cells linked to the diurnal cycle of solar heating). As a result, depending on the event, MAPLE forecasts lose their skill after 4–12 h as reported by Germann et al. (2006). Consequently, daily series of MAPLE forecasts have been constructed not from a single 24-h run as done for the NWP models, but by combining a sequence of three 8-h forecasts initialized at 0000, 0800, and 1600 UTC. This dataset has been used for the analysis of MAPLE's depiction of the diurnal cycle with the aim of quantifying the part of the diurnal cycle that is explained by the motion of precipitation systems. That is, if we imagine the diurnal cycle as being composed of local changes in precipitation plus their transport, MAPLE captures the second effect.

Figure 9a shows the Hovmöller diagrams of MAPLE forecasts constructed with the 8-h nowcasts initialized at 0000, 0800, and 1600 UTC. That is, rainfall observations at 0000, 0800, and 1600 UTC have been extrapolated

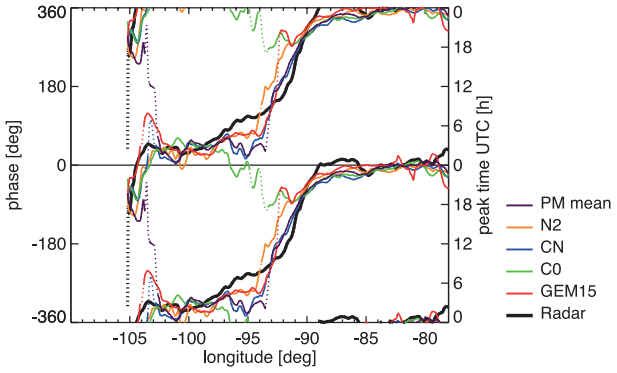

FIG. 8. Phase of the 24-h harmonic as function of longitude fitted to the Hovmöller diurnal cycle of average hourly rainfall intensity for the period 16 Apr–6 Jun 2008 (Figs. 6 h–n). Refer to the legend for the source of the various curves. The dotted lines indicate that the harmonic explains less than 10% of the variance of the signal, and hence is not considered significant.

with the motion fields estimated in the immediate past (i.e., precipitation intensities remain constant throughout the forecast). Similarly, Fig. 9b shows the corresponding Hovmöller diagram when MAPLE forecasts are initialized at 0100, 0900, and 1700 UTC. The differences between the two graphs reveal the impact of the initialization time, resulting in a significantly better performance of the forecasts initialized at 0100 UTC in the range 0100–0600 UTC. These nowcasts take advantage of the more mature stage of precipitation systems at initialization time (as can be seen in Fig. 9c), compared with those generated at 0000 UTC, which, on average, correspond to an earlier stage of precipitation organized in small-scale systems and with less well-defined trajectories. Thus, the diurnal cycle of precipitation in the longitudinal range 100°–89°W is mostly explained by the movement of precipitation systems from the lee side of the Rockies, and not by local convection initiation and dissipation.

There is another element that affects the performance of MAPLE: the same motion field, and therefore the same advection, is used over the entire forecast period (in our case, 8 h). Figure 8 shows that within 100°–92°W and between 0100 and 0800 UTC, the zonal motion of the systems is approximately constant, then changing at 0800 UTC, and again becoming constant between 1000 and 0000 UTC (see the slope of the black line in Fig. 8). Therefore it is expected that initializing MAPLE at 0800 UTC would result in precipitation systems moving slower than observed. Indeed, Figs. 9a,b confirm this result: the slope of the rainfall band at 95°W between 0800 and 1700 UTC is steeper than for radar observations (Fig. 9c).

As a measure of predictability, Germann and Zawadzki (2002) suggested using the lifetime (or decorrelation time) of precipitation systems, defined as the time lag required for the Lagrangian time correlation to fall below $1/e$. As MAPLE forecasts are based on Lagrangian persistence, their analysis allows us to investigate the dependence of their predictability on the time of day (Fig. 10). In general, lifetimes presented in Fig. 10 are consistently higher than the average value of 5.1 h determined by Germann et al. (2006) from 1424 h of precipitation over a similar season and domain size but for years between 1996 and 2001. The differences in accumulation window and resolution of the analyzed data, namely, our hourly accumulations at 32 km versus their instantaneous 4-km radar data, may at least in part explain this result. Figure 10 confirms a clear dependence of the lifetime of rainfall systems on initialization time, thus corroborating previous results. The skill of MAPLE forecasts initialized around 2000 UTC rapidly decays (the correlation decreases under $1/e$ after only 5.2 h). This time coincides with the average time of convection initiation in the foothills of the Rockies, which MAPLE cannot forecast. The maximum lifetime of 7.2 h occurs for forecasts initialized at 0100 UTC when the precipitation patterns have achieved a greater organization and their motion plays a more important role in their evolution. Whether these lifetimes are a measure of the predictability inherent to the actual precipitation systems or only attributable to the MAPLE nowcasts depends on the existence of a relationship between predictability by Lagrangian extrapolation and physical predictability (which is a question that remains unanswered).

5. Performance as function of the time of day

As in Part I, the diurnal variation of the skill of models and MAPLE in forecasting precipitation has been investigated. It is presented here in terms of the critical success index (CSI; see, e.g., Wilks 1995), correlation, bias (i.e., the ratio between forecasted and observed coverage), and root-mean-square error (RMSE) computed between observations and forecasts over the 32-km grid within the analysis domain (section 2d) as a function of time from initialization up to 30 h (Fig. 11). Correlation has been calculated for the rainfall field in logarithmic units and without subtracting the mean (as in Germann and Zawadzki 2002), the CSI and the bias are presented for a threshold of 0.2 mm h^{-1}, and the RMSE is computed in terms of hourly intensities (in mm).

Since MAPLE was run to generate 8-h forecasts, Fig. 11 displays the mean scores for four runs, initialized every 8 h. For the first hour after initialization, MAPLE shows very good CSI and correlation, but these scores quickly decay with forecasting time. From the verification in terms of the correlation coefficient, we deduce average lifetimes

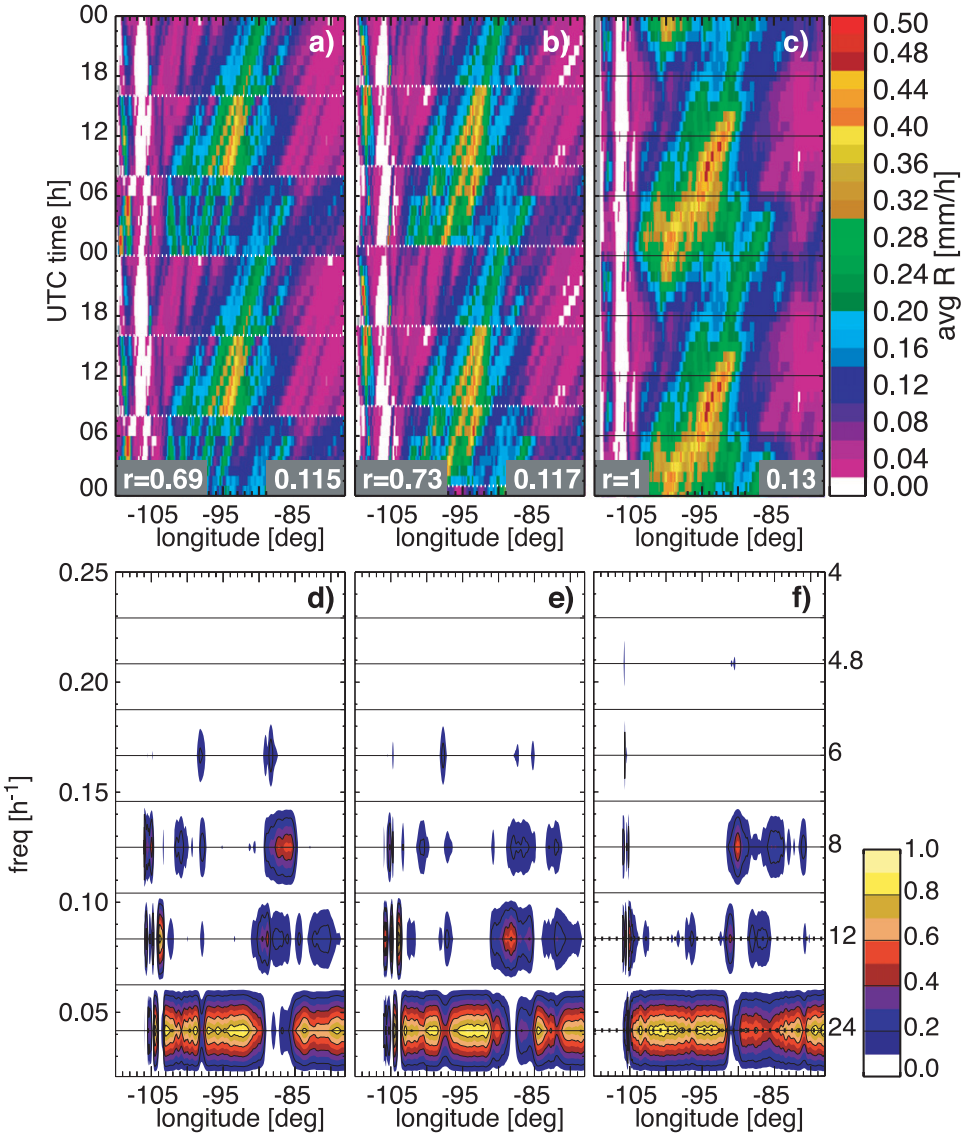

FIG. 9. Hovmöller diagrams of the average diurnal cycle of hourly rainfall intensity corresponding to (a) MAPLE forecasts initialized at 0000, 0800, and 1600 UTC; (b) MAPLE forecasts initialized at 0100, 0900, and 1700 UTC; and (c) radar observations. The correlation coefficients computed in the Hovmöller domain between MAPLE forecasts and radar observations are shown in the bottom-left corners, and the average rainfall intensities in mm h^{-1} are shown in the bottom-right corners. (d)–(f) The normalized power spectra of the Hovmöller diagrams of (a)–(c) as a function of longitude.

of 6.5, 6.4, and 5.5 h for the forecasts initialized at 0000, 0800, and 1600 UTC, respectively (Fig. 11).

The spinup time (defined as the time required for the forecast skill to stabilize) is estimated to be about 6–7 h for C0, and only 2–3 h for GEM15. The CSI and correlation then stabilize at a nearly constant performance for lead times between 8 and 30 h (as found by Lin et al. 2005; Clark et al. 2009). Because of radar data assimilation, SSEF members CN and N2 and the PM mean yield high CSI and correlation for the first forecast hour, but these scores decrease quite rapidly during the second hour. This rapid decrease in skill suggests an important difference between the atmospheric state represented by the ICs as obtained with a 3D-Var assimilation system and the atmospheric state represented in the model. The adjustment of the model to these ''imperfect'' ICs results in forecasts rapidly diverging from radar observations as time progresses. The time taken by these models to exhibit similar performance as GEM15 and C0 represents the duration of the effect of assimilating radar

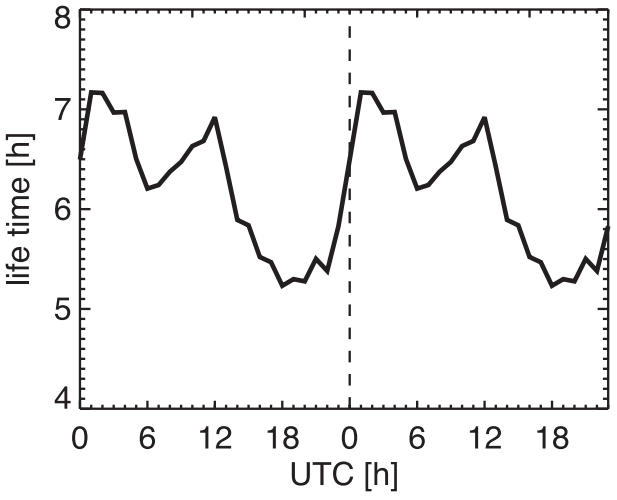

FIG. 10. Lifetime of rainfall systems as a function of time of the day as estimated from MAPLE forecasts. The 24-h cycle is plotted twice for clarity.

observations, which, according to Fig. 11, is about 15 h. The statistical significance of differences in CSI and correlation between various models was evaluated using the resampling methodology of Hamill (1999). Results of this evaluation are presented in Fig. 12 for the differences in CSI between C0, CN, GEM15, PM mean, and MAPLE (the results are very similar for correlation coefficients and hence not shown). Figure 12a shows that the difference in CSI between GEM15 and C0 is only significant for the first 2 h, when GEM15 shows better scores (probably due to better initial conditions). On the other hand, because of the radar data assimilation, CN is significantly more skillful than GEM15 for the first 3 h of the forecasts (Fig. 12d), while afterward the differences in CSI and correlation between GEM and CN are not statistically significant. Whereas Fig. 11 shows that CN exhibits better CSI and correlation than C0 throughout the forecast, it can be seen in Fig. 12 that the differences in skill are significant for the first 7 h. In addition, the PM mean becomes significantly better than CN only after 7 h (Fig. 12e), by smoothing the errors of the individual members. For lead times up to 7 h, the assimilation of radar data improves the quality of forecasts and reduces the spread of the ensemble in terms of precipitation by bringing all members closer to observations at IC (note that C0, which does not assimilate radar data, is not included in the calculation of the PM mean).

With respect to model–MAPLE comparison, Fig. 12f shows that MAPLE is significantly better than CN only for the first 2 h, while it outperforms C0 for the first 4 h.

Figure 11c shows that all models, except C0 during its spinup time, reproduce remarkably well within the ±25% limits the time dependency of precipitation coverage during the first 15 h of the forecasts. However, the

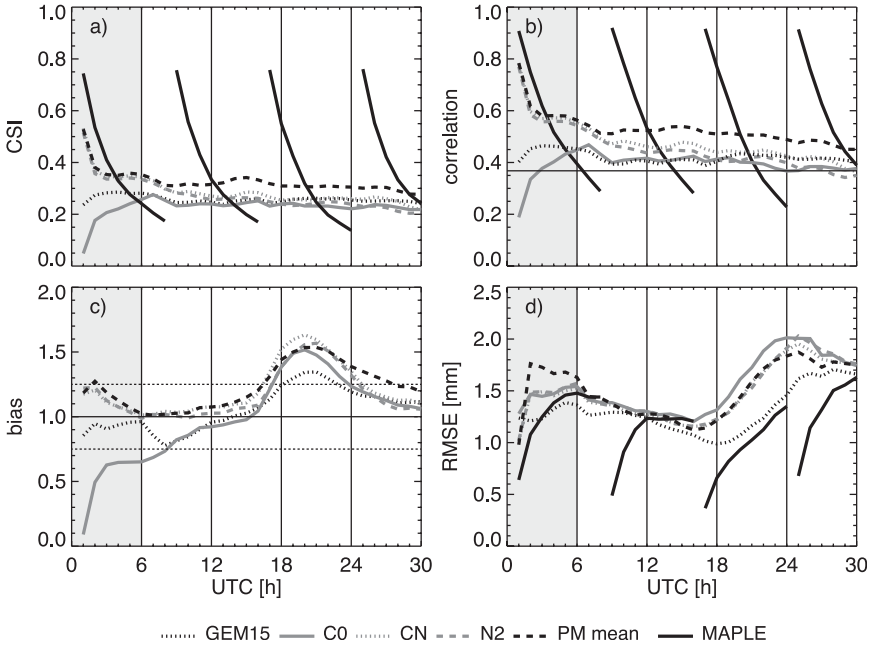

FIG. 11. Overall performance of the models as a function of the time of day: (a) critical success index for hourly intensities over 0.2 mm h^{-1}, (b) correlation between forecasted and verification rainfall in logarithmic units, (c) biases for intensities over 0.2 mm h^{-1}, and (d) root-mean-square error of hourly intensities.

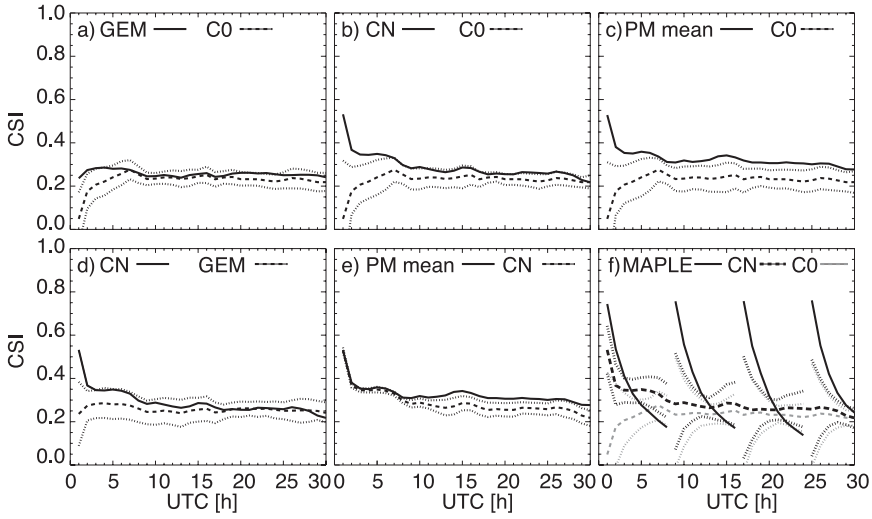

FIG. 12. Statistical significance of differences in CSI between different pairs of models (indicated in the title of each): (a) C0 and GEM; (b) C0 and CN; (c) C0 and PM mean; (d) GEM − CN; (e) CN − PM mean; (f) C0, CN, and MAPLE for hourly rainfall intensities over 0.2 mm h^{-1} as a function of the time of day. The dashed line in each shows the CSI corresponding to the reference model, and the solid line corresponds to the CSI of the other model. The dotted lines show the intervals for which the differences in CSI are considered significant (for a level $\alpha = 0.05$) such that when the solid line is above (below) the dotted lines the compared model (solid line) is significantly better (worse) than the reference model (dashed line).

bias has a marked diurnal cycle for each of the models (which is not observed with the CSI and correlation), with the maximum bias coinciding with the maximum precipitation coverage depicted by radar observations (see Fig. 2 and Part I). Note that for reasons already mentioned (section 3), the PM mean overestimates precipitation coverage more than any of the three analyzed SSEF members.

Finally, Fig. 11d shows very similar RMSE scores for the different model configurations for about 15 h. Beyond this lead time, GEM15 benefits from the smaller bias to obtain significantly better RMSE scores. The significance analyses show that the RMSE of the PM mean is comparable to that of the individual SSEF members, the best performance in terms of correlation being counterbalanced by the larger biases that affect the PM mean.

6. Conclusions

Using 24 days of precipitation from 16 April to 6 June 2008, the present study repeats the analysis of Part I with a focus on the intercomparison of a variety of NWP models and of an extrapolation-based nowcasting technique, and on their ability to capture the diurnal cycle of precipitation.

As discussed in Part I, synoptic forcing plays a more important role in the initiation and evolution of rainfall in spring than during summer. Thus, the evolution of convection induced by thermal forcing, regularly occurring in the foothills of the western Rockies during this time period is strongly influenced by large-scale systems. This results in longer-lived and organized precipitation systems with consistent timing and motion characteristics.

The comparison of the average Hovmöller diagrams derived from the 6–30-h forecasts indicates that GEM15 and the 4-km explicit convection SSEF system possess similar skill at depicting the longitudinal dependence of the diurnal cycle of precipitation. Both GEM15 and the SSEF reproduce the average timing of precipitation initiation along the foothills of the Rockies, and the corridor along which precipitation travels, but all model configurations suffer from the general overprediction of precipitation coverage and amounts. Bryan et al. (2003) and Clark et al. (2007) suggest that this inadequacy could be attributed to the failure of the models to resolve convective instability by subcloud-scale eddies. All models incorrectly delay the dissipation of precipitation systems in the eastern part of the domain and generate erratic positional and timing errors.

The PM mean better reproduces the diurnal cycle of precipitation than any of the members. In addition, the use of the probability-matching procedure smoothens the low-occurrence features predicted by the individual members, while preserving the distribution of rainfall intensities of the ensemble.

The comparison between forecasts and observations in terms of CSI and correlation shows that GEM15 and the non-radar-assimilating 4-km SSEF member C0 have, on average, a similar performance with time of the day over the common 32-km grid. These results agree with the findings of Mass et al. (2002), who concluded that moving to high-resolution models with explicit convection does not significantly improve the prediction of synoptic-scale systems that are more frequent in spring, although it may produce better-defined mesoscale features. However, our results show a superior performance of the other analyzed SSEF members during the first 0–7 h of the forecast, which can be explained by the assimilation of radar data (as similarly obtained by Kain et al. 2010). Also, the PM mean benefits from radar data assimilation to produce the best CSI and correlation scores.

MAPLE's depiction of the diurnal cycle of precipitation has also been included. The objective of this analysis is to describe the component of the diurnal cycle that can be explained solely by the observed motion of precipitation systems. Hovmöller diagrams show that three periods of Lagrangian persistence initiated at 0100, 0900, and 1700 UTC reproduce remarkably well the features of the band in the longitudinal range 95°–85°W. This suggests that to a reasonable approximation the diurnal cycle of precipitation within this longitudinal range can be explained by the steady motion of precipitation systems initiated in the western portion of the domain and traveling across the continent, and not by local convection initiation and dissipation (as also shown in Carbone et al. 2002 and Part I). As seen in section 3, the NWP models have some difficulty in reproducing the characteristics of this signal.

Since MAPLE neglects precipitation growth and decay, its performance is highly dependent on the initialization time: the best results are obtained when MAPLE is initialized at 0100 UTC due to the more mature stage of precipitation systems that start traveling to the east, while the worst performance occurs at 1900–2000 UTC, coinciding with the initiation of convection at the foothills of the Rockies, which MAPLE is unable to reproduce. It would be interesting to investigate whether NWP models would exhibit a similar dependence on initialization time.

MAPLE nowcasts for the 0000 UTC run show significantly better skill than the radar data assimilating SSEF members for 3 h; while after the first 5 h CN is significantly more skillful than MAPLE. On the other hand, it takes about 5 h for GEM15 and the non-radar-assimilating SSEF member C0 to exhibit a similar performance, while C0 is significantly better than MAPLE only after 7 h. While a Lagrangian extrapolation system such as MAPLE would still be preferred during the first 3 h, the results mentioned above remain encouraging for the use of NWP models that are assimilating radar data for precipitation nowcasting. Beyond the first 6 h, model skill scores stay almost constant with lead time (section 5), while the new initializations of MAPLE produce better rainfall forecasts than models for the next 4–6 h. Similarly, Kilambi and Zawadzki (2005) and Lin et al. (2005) found that MAPLE outperformed earlier versions of GEM and WRF (without radar data assimilation) for about 6 h. Although the comparison of the NWP forecasts with MAPLE forecasts initialized at different times would at first appear to be meaningless, it may still be of interest from the practical point of view.

We recognize that the selection as the verification ground truth of the same radar-based rainfall maps also used to generate MAPLE nowcasts provides an advantage to MAPLE, especially when compared with the SSEF members that assimilate 3D reflectivity data from individual radars (see section 2a). Obviously the radar-estimated rainfall and the rainfall at the initial time are identical for MAPLE, while this is not the case for the model-predicted rainfall in CN, even though it has an initial reflectivity field that should be very close to the one used as reference. Although the choice of the verification product has been done after assessing a number of alternatives, the present results should nonetheless be interpreted with caution considering that the 2.5-km CAPPI (see section 2c) is not a perfect estimate of precipitation at the ground.

The results presented are expected to be seasonally dependent. For the warm season, the studies Clark et al. (2007) found parameterized convection models to be less accurate than convection-allowing models. Similarly, in Part I we speculated that in spring GEM15 benefits from the predominance of synoptic-scale forcing, while in summer GEM15 shows clear difficulties in reproducing the west–east motion component of precipitation systems induced by thermal forcing. Data for the CAPS SSEF are not yet available for periods other than spring, and, thus, it is not possible to make a similar comparison using a convection-allowing model. Also, we point out that the comparison has been performed over a 32-km grid and, consequently, no conclusion can be made on model performance at smaller scales. Similarly, we emphasize the tentative nature of the results presented here due to the limited length of the analyzed dataset. Fritsch and Carbone (2004) stress the need of validating such state-of-the-art NWP systems against multiyear remote sensing data.

Acknowledgments. This work was made possible by the support of Environment Canada to the J.S. Marshall Radar Observatory. The GEM15 forecasts were provided by the Canadian Meteorological Centre. The CAPS SSEF

forecasts were produced mainly under the support of a grant from the NOAA CSTAR program, and the 2008 ensemble forecasts were produced at the Pittsburgh Supercomputer Center. Kevin Thomas, Jidong Gao, Keith Brewster, and Yunheng Wang of CAPS made significant contributions to the forecasting efforts. The first author is supported by a grant of the Ramón y Cajal Program of the Spanish Ministry of Science and Innovation. The authors thank Dr. Aldo Bellon for his thorough review of the manuscript. We also wish to acknowledge an anonymous reviewer for helpful insights and comments.

REFERENCES

Bélair, S., L.-P. Crevier, J. Mailhot, B. Bilodeau, and Y. Delage, 2003a: Operational implementation of the ISBA land surface scheme in the Canadian regional weather forecast model. Part I: Warm season results. *J. Hydrometeor.,* **4,** 352–370.

——, R. Brown, J. Mailhot, B. Bilodeau, and L.-P. Crevier, 2003b: Operational implementation of the ISBA land surface scheme in the Canadian regional weather forecast model. Part II: Cold season results. *J. Hydrometeor.,* **4,** 371–386.

——, J. Mailhot, C. Girard, and P. Vaillancourt, 2005: Boundary layer and shallow cumulus clouds in a medium-range forecast of a large-scale weather system. *Mon. Wea. Rev.,* **133,** 1938–1960.

Brewster, K., M. Hu, M. Xue, and J. Gao, 2005: Efficient assimilation of radar data at high resolution for short-range numerical weather prediction. Preprints, *WWRP Int. Symp. on Nowcasting and Very Short Range Forecasting,* Toulouse, France, Météo-France, 3.06. [Available online at http://twister.ou.edu/papers/BrewsterWWRP_Nowcasting.pdf.]

Bryan, G. H., J. C. Wyngaard, and J. M. Fritsch, 2003: Resolution requirements for the simulation of deep moist convection. *Mon. Wea. Rev.,* **131,** 2394–2416.

Carbone, R. E., J. D. Tuttle, D. A. Ahijevych, and S. B. Trier, 2002: Inferences of predictability associated with warm season precipitation episodes. *J. Atmos. Sci.,* **59,** 2033–2056.

Clark, A. J., W. A. Gallus, and T. C. Chen, 2007: Comparison of the diurnal precipitation cycle in convection-resolving and non-convection-resolving mesoscale models. *Mon. Wea. Rev.,* **135,** 3456–3473.

——, ——, M. Xue, and F. Y. Kong, 2009: A comparison of precipitation forecast skill between small convection-allowing and large convection-parameterizing ensembles. *Wea. Forecasting,* **24,** 1121–1140.

Coniglio, M. C., K. L. Elmore, J. S. Kain, S. J. Weiss, M. Xue, and M. L. Weisman, 2010: Evaluation of WRF model output for severe-weather forecasting from the 2008 NOAA Hazardous Weather Testbed Spring Experiment. *Wea. Forecasting,* **25,** 408–427.

Côté, J., S. Gravel, A. Méthot, A. Patoine, M. Roch, and A. Staniforth, 1998: The operational CMC-MRB Global Environmental Multiscale (GEM) model. Part I: Design considerations and formulation. *Mon. Wea. Rev.,* **126,** 1373–1395.

Dai, A., and K. E. Trenberth, 2004: The diurnal cycle and its depiction in the Community Climate System Model. *J. Climate,* **17,** 930–951.

——, F. Giorgi, and K. E. Trenberth, 1999: Observed and model-simulated diurnal cycles of precipitation over the contiguous United States. *J. Geophys. Res.,* **104** (D6), 6377–6402.

Davis, C. A., K. W. Manning, R. E. Carbone, S. B. Trier, and J. D. Tuttle, 2003: Coherence of warm-season continental rainfall in numerical weather prediction models. *Mon. Wea. Rev.,* **131,** 2667–2679.

Du, J., J. McQueen, G. DiMego, Z. Toth, D. Jovic, B. Zhou, and H. Chuang, 2006: New dimension of NCEP Short-Range Ensemble Forecasting (SREF) system: Inclusion of WRF members. Preprints, *WMO Expert Team Meeting on Ensemble Prediction Systems,* Exeter, United Kingdom, WMO, 5 pp. [Available online at http://www.emc.ncep.noaa.gov/mmb/SREF/WMO06_full.pdf.]

Dudhia, J., 1989: Numerical study of convection observed during the winter monsoon experiment using a mesoscale two-dimensional model. *J. Atmos. Sci.,* **46,** 3077–3107.

Ebert, E. E., 2001: Ability of a poor man's ensemble to predict the probability and distribution of precipitation. *Mon. Wea. Rev.,* **129,** 2461–2480.

Ek, M. B., K. E. Mitchell, Y. Lin, E. Rogers, P. Grunmann, V. Koren, G. Gayno, and J. D. Tarpley, 2003: Implementation of Noah land surface model advances in the National Centers for Environmental Prediction operational mesoscale Eta model. *J. Geophys. Res.,* **108,** 8851, doi:10.1029/2002JD003296.

Ferrier, B. S., Y. Jin, Y. Lin, T. Black, E. Rogers, and G. DiMego, 2002: Implementation of a new grid-scale cloud and rainfall scheme in the NCEP Eta Model. Preprints, *19th Conf. on Weather Analysis and Forecasting/15th Conf. on Numerical Weather Prediction,* San Antonio, TX, Amer. Meteor. Soc., 10.1. [Available online at http://ams.confex.com/ams/SLS_WAF_NWP/techprogram/paper_47241.htm.]

Fouquart, Y., and B. Bonnel, 1980: Computations of solar heating of the earth's atmosphere: A new parameterization. *Contrib. Atmos. Phys.,* **53,** 35–62.

Fritsch, J. M., and R. E. Carbone, 2004: Improving quantitative precipitation forecasts in the warm season. *Bull. Amer. Meteor. Soc.,* **85,** 955–965.

Gao, J., M. Xue, K. Brewster, and K. K. Droegemeier, 2004: A three-dimensional variational data analysis method with recursive filter for Doppler radars. *J. Atmos. Oceanic Technol.,* **21,** 457–469.

Garand, L., 1983: Some improvements and complements to the infrared emissivity algorithm including a parameterization of the absorption in the continuum region. *J. Atmos. Sci.,* **40,** 230–244.

Germann, U., and I. Zawadzki, 2002: Scale-dependence of the predictability of precipitation from continental radar images. Part I: Description of the methodology. *Mon. Wea. Rev.,* **130,** 2859–2873.

——, ——, and B. Turner, 2006: Predictability of precipitation from continental radar images. Part IV: Limits to prediction. *J. Atmos. Sci.,* **63,** 2092–2108.

Hamill, T. M., 1999: Hypothesis tests for evaluating numerical precipitation forecasts. *Wea. Forecasting,* **14,** 155–167.

Hong, S.-Y., and J.-O. J. Lim, 2006: The WRF Single-Moment 6-Class Microphysics Scheme (WSM6). *J. Korean Meteor. Soc.,* **42,** 129–151.

Hu, M., M. Xue, and K. Brewster, 2006a: 3DVAR and cloud analysis with WSR-88D level-II data for the prediction of Fort Worth tornadic thunderstorms. Part I: Cloud analysis and its impact. *Mon. Wea. Rev.,* **134,** 675–698.

——, ——, J. Gao, and K. Brewster, 2006b: 3DVAR and cloud analysis with WSR-88D level-II data for the prediction of Fort Worth tornadic thunderstorms. Part II: Impact of radial velocity analysis via 3DVAR. *Mon. Wea. Rev.,* **134,** 699–721.

Janjic, Z. I., 2001: Nonsingular implementation of the Mellor–Yamada level 2.5 scheme in the NCEP Meso-model. NCEP Office Note 437, NOAA/NWS, 61 pp.

——, 2003: A nonhydrostatic model based on a new approach. *Meteor. Atmos. Phys.,* **82,** 271–285.

Janowiak, J. E., V. J. Dagostaro, V. E. Kousky, and R. J. Joyce, 2007: An examination of precipitation in observations and model forecasts during NAME with emphasis on the diurnal cycle. *J. Climate,* **20,** 1680–1692.

Kain, J. S., and J. M. Fritsch, 1990: A one-dimensional entraining detraining plume model and its application in convective parameterization. *J. Atmos. Sci.,* **47,** 2784–2802.

——, and ——, 1993: Convective parameterization for mesoscale models: The Kain–Fritsch scheme. *The Representation of Cumulus Convection in Numerical Models, Meteor. Monogr.,* No. 24, Amer. Meteor. Soc., 165–170.

——, and Coauthors, 2010: Assessing advances in the assimilation of radar data and other mesoscale observations within a collaborative forecasting-research environment. *Wea. Forecasting,* **25,** 1510–1521.

Kilambi, A., and I. Zawadzki, 2005: An evaluation of ensembles based upon MAPLE precipitation nowcasts and NWP precipitation forecasts. Preprints, *32nd Conf. on Radar Meteorology,* Albuquerque, NM, Amer. Meteor. Soc., P3R.4. [Available online at http://ams.confex.com/ams/pdfpapers/96982.pdf.]

Knievel, J. C., D. A. Ahijevych, and K. W. Manning, 2004: Using temporal modes of rainfall to evaluate the performance of a numerical weather prediction model. *Mon. Wea. Rev.,* **132,** 2995–3009.

Kong, F., and Coauthors, 2008: Real-time storm-scale ensemble forecast 2008 Spring Experiment. Preprints, *24th Conf. on Severe Local Storms,* Savannah, GA, Amer. Meteor. Soc., 12.3. [Available online at http://ams.confex.com/ams/24SLS/techprogram/paper_141827.htm.]

Laroche, S., and I. Zawadzki, 1995: Retrievals of horizontal winds from single-Doppler clear-air data by methods of cross-correlation and variational analysis. *J. Atmos. Oceanic Technol.,* **12,** 721–738.

——, P. Gauthier, J. St.-James, and J. Morneau, 1999: Implementation of a 3D variational data assimilation system at the Canadian Meteorological Center. Part II: The regional analysis. *Atmos.–Ocean,* **37,** 281–307.

Lin, C., S. Vasic, A. Kilambi, B. Turner, and I. Zawadzki, 2005: Precipitation forecast skill of numerical weather prediction models and radar nowcasts. *Geophys. Res. Lett.,* **32,** L14801, doi:10.1029/2005GL023451.

Mailhot, J., and Coauthors, 2006: The 15-km version of the Canadian regional forecast system. *Atmos.–Ocean,* **44,** 133–149.

Mass, C. F., D. Ovens, K. Westrick, and B. A. Colle, 2002: Does increasing horizontal resolution produce more skillful forecasts? The results of two years of real-time numerical weather prediction over the Pacific Northwest. *Bull. Amer. Meteor. Soc.,* **83,** 407–430.

Mellor, G. L., and T. Yamada, 1982: Development of a turbulence closure model for geophysical fluid problems. *Rev. Geophys.,* **20,** 851–875.

Mlawer, E. J., S. J. Taubman, P. D. Brown, M. J. Iacono, and S. A. Clough, 1997: Radiative transfer for inhomogeneous atmospheres: RRTM, a validated correlated-k model for the longwave. *J. Geophys. Res.,* **102,** 16 663–16 682.

Noh, Y., W. G. Cheon, S. Y. Hong, and S. Raasch, 2003: Improvement of the k-profile model for the planetary boundary layer based on large eddy simulation data. *Bound.-Layer Meteor.,* **107,** 401–427.

Schwartz, C. S., and Coauthors, 2009: Next-day convection-allowing WRF model guidance: A second look at 2-km versus 4-km grid spacing. *Mon. Wea. Rev.,* **137,** 3351–3372.

——, and Coauthors, 2010: Toward improved convection-allowing ensembles: Model physics sensitivities and optimizing probabilistic guidance with small ensemble membership. *Wea. Forecasting,* **25,** 263–280.

Skamarock, W. C., and Coauthors, 2008: A description of the Advanced Research WRF Version 3. NCAR Tech Note NCAR/TN-475+STR, 125 pp. [Available online at http://www.mmm.ucar.edu/wrf/users/docs/arw_v3.pdf.]

Sundqvist, H., 1978: A parameterization scheme for non-convective condensation including prediction of cloud water content. *Quart. J. Roy. Meteor. Soc.,* **104,** 677–690.

Surcel, M., M. Berenguer, I. Zawadzki, M. Xue, and F. Kong, 2009: The diurnal cycle of precipitation in radar observations, model forecasts and MAPLE nowcasts. Preprints, *34th Conf. on Radar Meteorology,* Williamsburg, VA, Amer. Meteor. Soc., P14.6. [Available online at http://ams.confex.com/ams/pdfpapers/155493.pdf.]

——, ——, and ——, 2010: The diurnal cycle of precipitation from continental radar mosaics and numerical weather prediction models. Part I: Methodology and seasonal comparison. *Mon. Wea. Rev.,* **138,** 3084–3106.

Tao, W. K., and Coauthors, 2003: Microphysics, radiation and surface processes in the Goddard Cumulus Ensemble (GCE) model. *Meteor. Atmos. Phys.,* **82,** 97–137.

Thompson, G., P. R. Field, R. M. Rasmussen, and W. D. Hall, 2008: Explicit forecasts of winter precipitation using an improved bulk microphysics scheme. Part II: Implementation of a new snow parameterization. *Mon. Wea. Rev.,* **136,** 5095–5115.

Weisman, M. L., C. Davis, W. Wang, K. W. Manning, and J. B. Klemp, 2008: Experiences with 0-36-h explicit convective forecasts with the WRF-ARW model. *Wea. Forecasting,* **23,** 407–437.

Wilks, D. S., 1995: *Statistical Methods in Atmospheric Sciences.* International Geophysics Series, Vol. 59, Academic Press, 467 pp.

Xue, M., D.-H. Wang, J.-D. Gao, K. Brewster, and K. K. Droegemeier, 2003: The Advanced Regional Prediction System (ARPS), storm-scale numerical weather prediction and data assimilation. *Meteor. Atmos. Phys.,* **82,** 139–170.

——, and Coauthors, 2008: CAPS realtime storm-scale ensemble and high-resolution forecasts as part of the NOAA Hazardous Weather Testbed 2008 Spring Experiment. Preprints, *24th Conf. on Severe Local Storms,* Savannah, GA, Amer. Meteor. Soc., 12.2. [Available online at http://ams.confex.com/ams/24SLS/techprogram/paper_142036.htm.]

——, and Coauthors, 2009: CAPS realtime 4-km multi-model convection-allowing ensemble and 1-km convection-resolving forecasts for the NOAA hazardous weather testbed 2009 spring testbed. Preprints, *23rd Conf. on Weather Analysis and Forecasting/19th Conf. on Numerical Weather Prediction,* Omaha, NE, Amer. Meteor. Soc., 16A.2. [Available online at http://ams.confex.com/ams/23WAF19NWP/techprogram/paper_154323.htm.]

Zhang, J., K. Howard, and J. J. Gourley, 2005: Constructing three-dimensional multiple-radar reflectivity mosaics: Examples of convective storms and stratiform rain echoes. *J. Atmos. Oceanic Technol.,* **22,** 30–42.